

We present the BMW-*Chandra* source catalogue drawn from essentially all *Chandra* ACIS-I pointed observations with an exposure time in excess of 10 ks public as of March 2003 (136 observations). Using the wavelet detection algorithm developed by Lazzati et al. (1999) and Campana et al. (1999), which can characterise both point-like and extended sources, we identified 21325 sources. Among them, 16758 are serendipitous, i.e. not associated with the targets of the pointings, and do not require a non-automated analysis. This makes our catalogue the largest compilation of *Chandra* sources to date. The 0.5–10 keV absorption corrected fluxes of these sources range from $\sim 3 \times 10^{-16}$ to 9×10^{-12} erg cm $^{-2}$ s $^{-1}$ with a median of 7×10^{-15} erg cm $^{-2}$ s $^{-1}$. The catalogue consists of count rates and relative errors in three energy bands (total, 0.5–7 keV; soft, 0.5–2 keV; and hard, 2–7 keV), and source positions relative to the highest signal-to-noise detection among the three bands. The wavelet algorithm also provides an estimate of the extension of the source. We include information drawn from the headers of the original files, as well, and extracted source counts in four additional energy bands, SB1 (0.5–1 keV), SB2 (1–2 keV), HB1 (2–4 keV), and HB2 (4–7 keV). We computed the sky coverage for the full catalogue and for a subset at high Galactic latitude ($|b| > 20^\circ$). The complete catalogue provides a sky coverage in the soft band (0.5–2 keV, S/N = 3) of ~ 8 deg 2 at a limiting flux of $\sim 10^{-13}$ erg cm $^{-2}$ s $^{-1}$, and ~ 2 deg 2 at a limiting flux of $\sim 10^{-15}$ erg cm $^{-2}$ s $^{-1}$. Furthermore, we present the results of the cross-match with existing catalogues at different wavelengths (FIRST, IRAS, 2MASS, GSC2, and ChaMP). The total numbers of matches with the FIRST, IRASPSC, 2MASS, and GSC2 catalogues obtained after a closest-distance selection are 13, 87, 6700, and 4485, respectively.

The Brera Multi-scale Wavelet Chandra Survey[★]

I. Serendipitous source catalogue

P. Romano^{1,2}, S. Campana¹, R.P. Mignani³, A. Moretti¹, M. Mottini⁴, M.R. Panzera¹, and G. Tagliaferri¹

¹ INAF–Osservatorio Astronomico di Brera, Via E. Bianchi 46, 23807 Merate (LC), Italy

² INAF, Istituto di Astrofisica Spaziale e Fisica Cosmica, Via U. La Malfa 153, I-90146 Palermo, Italy

³ Mullard Space Science Laboratory, University College London, Holmbury St. Mary, Dorking, Surrey, RH5 6NT, United Kingdom

⁴ European Southern Observatory, Schwarzschild Straße 2, 85740 Garching bei München, Germany

Received ; accepted

ABSTRACT

Key words. Catalogs – X-rays: general

1. Introduction

The use of a wavelet transform (WT) as an X-ray detection algorithm was pioneered by Rosati et al. (1995; 1998) for the detection of extended sources in the Roentgen Satellite (*ROSAT*) Position Sensitive Proportional Counter (PSPC) fields and subsequently adopted by many groups (Grebenev et al. 1995; Damiani et al. 1997b; Pislari et al. 1997; Vikhlinin et al. 1998; Lazzati et al. 1998; Freeman, Kashyap, Rosner, & Lamb 2002). Differently from other WT-based algorithms, the Brera Multi-scale Wavelet (BMW, Lazzati et al. 1999; Campana et al. 1999) algorithm, which was developed to analyse *ROSAT* High Resolution Imager (HRI) data, automatically characterises each source through a multi-source χ^2 fitting with respect to a Gaussian model in the wavelet space. For these reasons it has also proven to perform well in crowded fields and in conditions of very low background (Lazzati et al. 1999).

The BMW was used to produce the BMW-HRI catalogue (Lazzati et al. 1999; Campana et al. 1999; Panzera et al. 2003), a catalogue of $\sim 29\,000$ sources detected with a probability of $\gtrsim 4.2\sigma$ and with a sky coverage of $732\,\text{deg}^2$ down to a limiting flux of $10^{-12}\,\text{erg cm}^{-2}\,\text{s}^{-1}$ and $10\,\text{deg}^2$ down to a limiting flux of $10^{-14}\,\text{erg cm}^{-2}\,\text{s}^{-1}$.

The BMW-HRI is being currently used for a number of scientific projects. Among preliminary results, an analysis of X-ray detected sources without obvious counterparts at other wavelengths, (a.k.a. blank field sources, Chierigato et al. 2005) has been carried out with the aim of identifying unusual objects, as well as a serendipitous X-ray survey of Lyon-Meudon Extragalactic Database (LEDA) normal galaxies (Tajer et al. 2005).

The BMW algorithm was modified to support the analysis of *Chandra* Advanced CCD Imaging Spectrometer (ACIS) images (Moretti et al. 2002), and has led to interesting results on the nature of the cosmic X-ray background (CXB, Campana et al.

2001; Moretti et al. 2003). Given the reliability and versatility of the BMW algorithm, we decided to apply it to a large sample of *Chandra* ACIS-I images, to take full advantage of the superb spatial resolution [$\sim 0''.5$ point-spread function (PSF) on-axis] of *Chandra* while being able to automatically analyse crowded fields and/or with very low background. We thus produced the Brera Multi-scale Wavelet *Chandra* source catalogue (BMW-C).

In this paper we present a pre-release of the BMW-C, which is based on a subset of the whole *Chandra* ACIS observations dataset, roughly corresponding to the first three years of operations.

Like the BMW-HRI, our catalogue provides source positions, count rates, extensions and relative errors. In addition, for all bright (100 counts in the 0.5–7 keV band) sources in the catalogue we extracted light curves which will be exploited in a search for periodic and non-periodic variability, as well as spectra to have an immediate spectral classification.

In Sect. 2 we describe the selection criteria of the *Chandra* fields and the resulting data sample. In Sect. 3 we describe the data processing, which includes data screening and correction, event list selections and energy band selections. In Sect. 4 we describe the wavelet detection algorithm and its application to the *Chandra* fields as well as the resulting source catalogue, the BMW-*Chandra* catalogue. In Sect. 5 we report the properties of the source sample, including their spatial extent fluxes, and the definition of our serendipitous sub-sample. In Sect. 6 we calculate the sky coverage of our survey. In Sect. 7 we compare our catalogue with the *Chandra* Multiwavelength Project (ChAMP, Kim et al. 2007a, and references therein) data. In Sect. 8 we describe preliminary results of the cross-matches between the BMW-*Chandra* and other catalogues at different wavelengths. Finally, in Sect. 9 we summarise our work and highlight the plan for future exploitation of the catalogue.

2. Data sample

Our choice of the *Chandra* fields favoured the ones that would maximise the sky area not occupied by the pointed targets, that is the fields where the original PI was interested in a single, pos-

Send offprint requests to: P. Romano; e-mail: romano@ifc.inaf.it

[★] The catalogue is available in electronic form at the CDS via web <http://cdsweb.u-strasbg.fr/cgi-bin/qcat?J/A+A/> or via anonymous ftp to cdsarc.u-strasbg.fr (130.79.128.5).

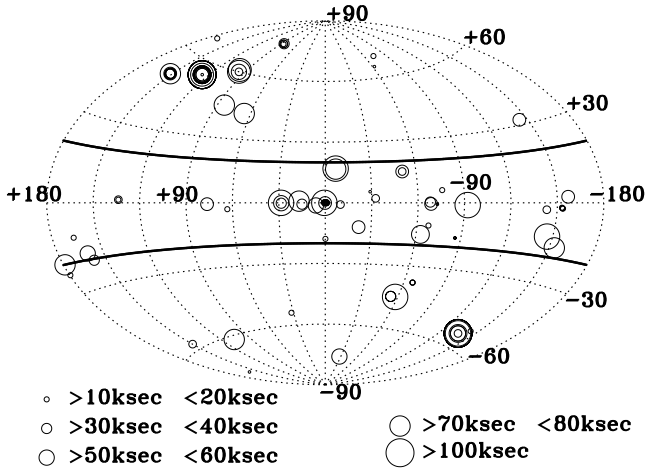


Fig. 1. Aitoff projection in Galactic coordinates of the 136 observations in the BMW-C catalogue. The size of each point is proportional to the exposure time, and the scale shows representative exposure times.

The thick lines are the limits of the high- and low-latitude sub-catalogues (see Sect. 5).

sibly point-like object centred in the field. We adopted the following criteria:

1. All ACIS-I [no grating, no High Resolution Camera (HRC) fields and in Timed Exposure mode] fields with exposure time in excess of 10 ks available by 2003 March were considered. Data from all four front-illuminated (FI) CCDs (I0, I1, I2, I3) were used.
2. We excluded fields dominated by extended sources [covering $\geq 1/9$ of the field of view (FOV)].
3. We excluded planet observations and supernova remnant observations.
4. We also excluded fields with bright point-like or high-surface brightness extended sources.
5. We put no limit on Galactic latitude, but we selected subsamples based on latitude at a later time.

The exclusion of bright point-like or high-surface brightness extended sources was dictated by the nature of our detection algorithm, which leads to an excessive number of spurious detections at the periphery of the bright source. This problem is common to most detection algorithms. Therefore, each field was visually inspected to check for such effects; where found, a conservatively large portion of the field was flagged (see Sect. 4). Of the 147 fields analysed, 11 ($\sim 7\%$) were discarded because of problems at various stages of the pipeline execution. The field relative to observation ID 634, for instance, was discarded because of the spacecraft wobbling during the exposure that caused the images of point sources to be elongated and to be detected as double. We eliminated observation ID 581 because the CCD I3 suffered from good time intervals inconsistent with the other CCDs, resulting in an anomalously high background (e.g., see Moretti et al. 2002). Furthermore, the observation IDs 316, 361, 950, 1302, 1872, 2269, and 2271 were eliminated because of problems at the detection stage. Finally, the fields relative to observation IDs 2365 and 1431 were discarded at the analysis stage because the aspect of the spacecraft changed during the observation. As a result, 136 fields reported successful completion of the pipeline. Figure 1 shows the Aitoff projection in Galactic coordinates of their positions. Table 1 lists the basic properties (observation ID,

Sequence number, coordinates of the target, etc.) of the fields included in our sample. We note that several fields were observed more than once. These fields were considered as different pointings, so that the number of distinct fields is 94 (see Sec. 6).

3. Data processing

Our pipeline is a combination of *Ciao*¹ tasks (data screening, image reduction, exposure map creation), IDL programs (additional data screening, wavelet detection core), tasks in the *HEASoft* package and UNIX shell scripts (drivers and house-keeping) that reduces and analyses the Level 2 (L2) data generated by the *Chandra* X-ray Center (CXC) standard data processing in a uniform fashion. The data (event list, the aspect solution, the aspect offset, and the bad pixel files) were downloaded using the *Chandra* Search and Retrieval tool (ChaSeR) from the *Chandra* Data Archive (CDA)², and were filtered to only include the standard event grades [Advanced Satellite for Cosmology and Astrophysics (ASCA) grades 0, 2, 3, 4, 6]. Since several *Chandra* data sets in the archive suffer from known aspect offsets as large as $2''$, we checked and corrected for this problem using the `fix_batch` Perl script by Tom Aldcroft³.

We applied energy filters to the offset-corrected L2 event list, and created soft (SB, 0.5–2.0 keV), hard (HB, 2.0–7.0 keV) and total (FB, 0.5–7.0 keV) band event files. The upper limit on our hard and total energy bands was chosen at 7 keV because at higher energy the background increases and the effective area decreases, producing lower signal-to-noise (S/N) data. Our results in the 0.5–10 keV band are then extrapolations from our findings in the 0.5–7 keV range (see Sects. 4.2, and 5.3).

Since the source detection strongly depends on the background rate, the data obtained during background flares were carefully removed. We created counts light curves with a time resolution that would allow ~ 400 counts per time bin, which typically correspond to ~ 1.4 ks and ~ 1.8 ks in the soft and hard bands, respectively, and excluded all time intervals during which the rate was more than 3σ of the mean rate. The mean fraction of exposure lost to background flares is 4%, comparable with 5% given by the ChaMP collaboration for FI chips (Kim et al. 2007a, 2004a). The effective exposure times reported in the catalogue (TEFF, see Table 1 and distribution shown in Fig. 2, median 31.8 ks), reflect these corrections.

Generally, hot/flickering pixels and bad columns are listed in the calibration database and eliminated by the *Ciao* tools. However, some remaining flickering pixels, probably due to the afterglow of cosmic rays or charged particles hitting the CCDs, occur and they were identified at this point. Following Tozzi et al. (2001), we defined as flickering each pixel that registered two events within the time of two consecutive frames. In each observation we eliminated all the events registered from that pixel, a procedure which is safe when no bright sources are present, such as is our case.

3.1. Total background map creation

The wavelet algorithm requires an accurate characterisation of the background of the images to process (see Sec. 4.1), since the WT detection is carried out on top of a map representing the image background (the total background map; Lazzati et al. 1999). The background in the ACIS-I images, in particular, is

¹ <http://cxc.harvard.edu/ciao/>

² <http://cxc.harvard.edu/cda/s+r.html>

³ http://cxc.harvard.edu/cal/ASPECT/fix_offset/fix_offset.cgi

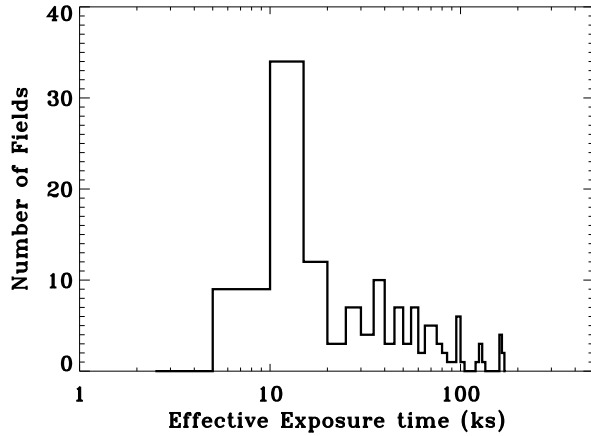


Fig. 2. Distribution of effective exposure times for the 136 observations.

the sum of two components, a cosmic X-ray background and a particle one (i.e., cosmic-ray-induced). The former suffers from vignetting and can be modelled as a power law of photon index $\Gamma = 1.4$ (Marshall et al. 1980; Moretti et al. 2003). The latter is not affected by vignetting, only depends on the temperature of the electronics, and can be modelled as a flat pattern with an inaccuracy within 10%⁴. For each field and for each of the three energy bands, we used the `merge_all` script to create exposure maps (adopting an input spectrum of a power law with photon index 1.4) and flat maps and then combined them.

4. Source detection and catalogue construction

4.1. The BMW-C algorithm

We used an updated version of the BMW detection algorithm that supports the analysis of *Chandra* ACIS images. The main steps of the algorithm can be summarised as follows (full details in Lazzati et al. 1998; Lazzati et al. 1999; Campana et al. 1999). The first step is the creation of the WT of the input image; the BMW WT is based on the discrete multi-resolution theory and on the “à trous” algorithm (Bijaoui & Giudicelli 1991), which differs from continuous-WT-based algorithms which can sample more scales at the cost of a longer computing time (Rosati et al. 1995; Grebenev et al. 1995; Damiani et al. 1997a). We used a Mexican hat mother-wavelet, which can be analytically approximated by the difference of two Gaussian functions (Slezak, Durret & Gerbal 1994). The WT decomposes each image into a set of sub-images, each of them carrying the information of the original image at a given scale. This property makes the WT well suited for the analysis of X-ray images, where the scale of sources is not constant over the field of view, because of the dependence of the PSF on the off-axis angle. We used 7 WT scales $a = [1, 2, 4, 8, 16, 32, 64]$ pixels to cover a wide range of source sizes, where a is the scale of the WT (Lazzati et al. 1999).

Candidate sources are identified as local maxima above the significance threshold in the wavelet space at each scale, so that a list is obtained at each scale, and then a cross-match is performed among the 7 lists to merge them. At the end of this step, we have a first estimate of source positions (the pixel with the highest WT coefficient), source counts (the local maximum of the WT) and a guess of the source extension (the scale at which the WT

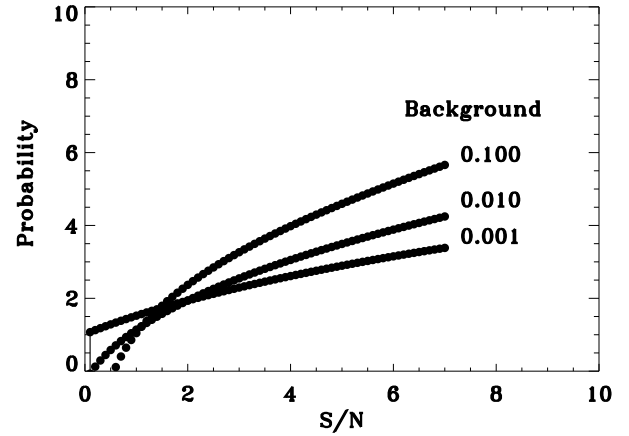


Fig. 3. Wavelet probability (or source significance in number of σ s) as a function of WT S/N and background value (counts, see Sect. 4.1).

is maximized). A critical parameter is the detection threshold which, in the context of WT algorithms, is usually fixed arbitrarily by the user in terms of expected spurious detections per field (Lazzati et al. 1998). The number of expected spurious detections as a function of the threshold value and for each scale was calculated by means of Monte Carlo simulations (Moretti et al. 2002). We ran the detection algorithm with a single significance threshold that corresponds to ~ 0.1 spurious detections per scale, hence (with 7 scales) ~ 0.7 spurious detections per field for each band in which we performed the detection. Given our sample of 136 fields, we expect a total of ~ 95 spurious sources in the catalogue.

The final step is the characterisation of the sources by means of a multi-source χ^2 minimization with respect to a Gaussian model source in the WT space. In order to fit the model on a set of independent data, the WT coefficients are decimated according to a scheme described in full in Lazzati et al. (1999).

The wavelet probability is defined as the confidence level at which a source is not a chance background fluctuation, given the background statistics and the specific field exposure time. This quantity is assessed via the S/N ratio in WT space. For each WT scale, the noise level is computed through numerical simulations of blank fields with the corresponding background (Lazzati et al. 1999), while the signal is the peak of the WT coefficients corresponding to the source. Figure 3 shows the wavelet probability as a function of WT S/N, and background value. In order to make this significance more easily comparable to other methods, confidence intervals are approximately expressed in units of the standard deviation σ for which a Gaussian distributed variable would give an equal probability of spurious detection (68%: 1σ ; 95%: 2σ , etc.). So, the values of the wavelet probability in the catalogue column WTPROBAB represent the number of σ ’s corresponding to the confidence level of that specific source.

We ran the detection algorithm on the central $\sim 8'$ portion of the source image at full resolution (rebin = 1, 1 pixel $\sim 0''.49$) and on the image rebinned by a factor of two outside (rebin = 2, 1 pixel $\sim 0''.98$). This strategy allowed us to optimize computer time, while preserving spatial information. Indeed, outside the $\sim 8'$ radius circle, the PSF radius that encircles 90% of the energy is $\geq 6''.5$, i.e., ≥ 6.6 rebinned pixels in the soft band and $\geq 7''.4$, i.e., ≥ 7.5 rebinned pixels in the hard band. In detail, a) we ran the detection on the images at rebin 2; b) we ran the detec-

⁴ http://xc.harvard.edu/cal/Links/Acis/acis/Cal_prods/bkgrnd/current/.

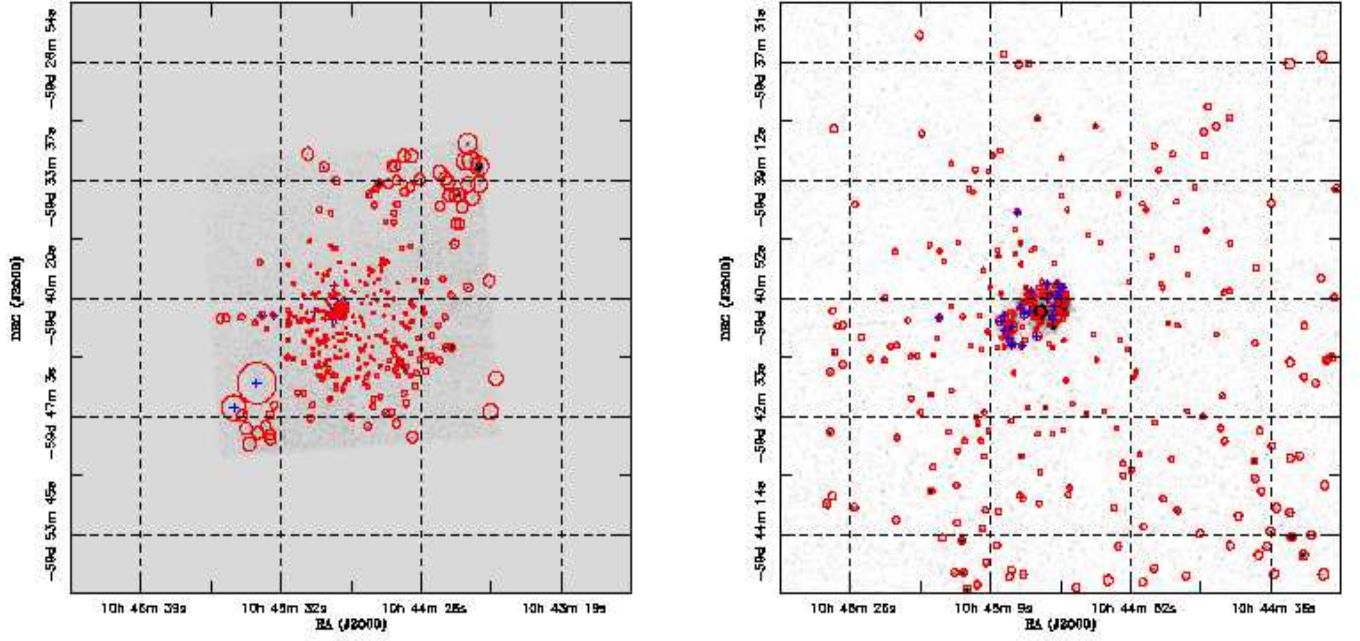


Fig. 4. Example of Detection. **Left:** the η Carinae full field (OBSID 50, SEQ_NUM 200019) at half resolution. The FOV is $\sim 33'$. The sources are represented with a size which is three times their Gaussian width. Note the complicated extended structure at the centre and the spurious detections along a readout streak (see Sect. 4.1) Crosses mark sources that the detection algorithm classifies as extended (e.g. bottom-left corner). **Right:** central portion of the field at full resolution. The FOV is $\sim 8.4'$ and the sources are represented with a size which is five times their Gaussian width.

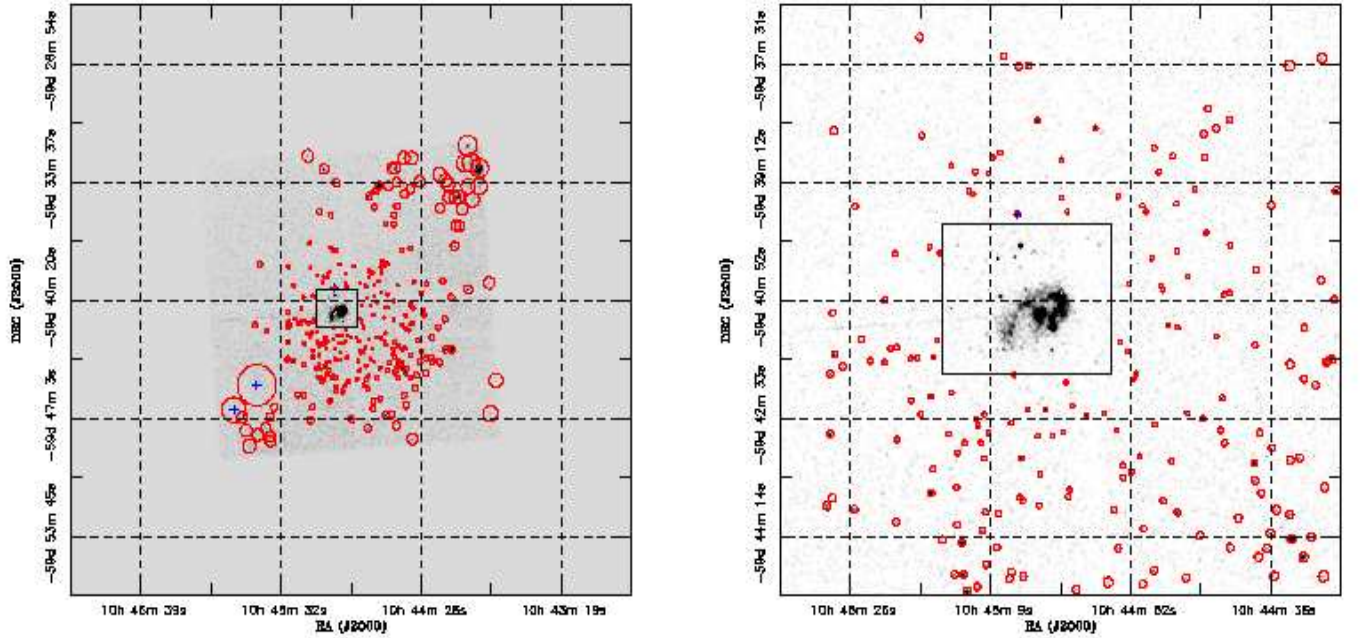


Fig. 5. Example of manual cleaning. The spurious sources along the readout streak were eliminated and the sources in the central portion of the image (contained within the box and not shown) were flagged.

tion in their inner 512×512 part (rebinned pixels, corresponding to $\sim 8.4 \times 8.4$) at the full resolution; c) we excluded the 480×480 pixel central part in the analysis at rebin 2 (rebinned pixels, corresponding to $\sim 7.8 \times 7.8$); d) we cross-matched the positions of the sources found at rebin 1 and 2 to exclude common double entries (sources were considered coincident if their distance was less than 6 times their width). We repeated this procedure for each of the three energy bands, and cross-matched the result-

ing source coordinates to form the definitive list (for coincident sources, the coordinates of the highest S/N one were kept).

A source extension, defined as the width of the best-fitting Gaussian model, was calculated for each band and the extension of the highest S/N among the three bands and the inner and outer regions was kept.

An example of the products of the pipeline is shown in Figs. 4 and 5, which represent the η Carinae field (OBSID 50, SEQ_NUM 200019), one of the most problematic observations

since it has a complicated extended structure at the centre as well as other data problems. Figure 4 (left) is the full image at rebin 2, with a FOV of $\sim 33'$. The sources are represented with circles with a size which is three times their Gaussian width. Note the spurious detections along a readout streak (photons detected during the readout in a field containing a bright source are clocked out in the wrong row and so have incorrect CHIPY values and show up as a streak along the column). Crosses mark sources that the detection algorithm classifies as extended. Figure 4 (right) shows the central portion of the field at full resolution. The FOV is $\sim 8.4'$, and the sources are represented with a size which is five times their Gaussian width for better presentation.

4.2. BMW-C catalogue

The pipeline produced a catalogue of source positions, count rates, counts, extensions, and relative errors, as well as the additional information drawn from the headers of the original files for a total of 21325 sources.

Source counts were corrected for vignetting using the exposure maps (see Sect. 3.1), i.e., by comparing the image counts at each source position with the average counts of the normalized exposure map within a PSF range. Furthermore, the source counts were corrected for PSF fitting, i.e., for using a Gaussian approximation of the PSF to fit the sources in the WT space. This latter correction was calculated by running the detection on the `psfsize` table in CALDB (`psfsize_2000830.fits`), using the PSF images at ~ 1.50 keV for the soft band PSF and at ~ 4.51 keV for the hard band PSF, and calculating the percentage of counts lost with the Gaussian approximation in the WT detection.

Errors were calculated in two ways: following Grebenev et al. (1995), appropriate for sufficiently high values of the background and source counts ($\gtrsim 5 \times 10^{-2}$ counts/pixel), and using basic statistic expressions. In the latter case, assuming a Gaussian shaped distribution of N photons of width (WIDTH) Δ , the positional errors in x and y (X_POS_E , Y_POS_E) are limited by $\sigma_x \approx \sigma_y \approx \Delta / \sqrt{N-1}$, the total positional error (T_POS_ER) is $\sigma_t \approx \sqrt{\sigma_x^2 + \sigma_y^2}$, the error on the total number of counts is given by Poisson statistics $\sigma_N \approx \sqrt{N}$, and the intrinsic limit on the width estimate is $\sigma_\Delta \approx 0.5 \Delta / \sqrt{N-1}$ (see detailed discussion in Lazzati et al. 1999). The largest of the values derived using the two methods is adopted. As an example, the distribution of the total positional error is shown in Fig. 6 for the 16834 sources that do not require a more in-depth, non-automated analysis (see below). We note that the absolute source position in *Chandra* observations has an uncertainty radius of $0''.6$ at 90% confidence level (CL), and of $0''.8$ at 99% CL⁵. These values were calculated by measuring the distances between the *Chandra* X-ray source positions and the corresponding optical/radio counterpart positions from the Tycho2 (Høg et al., 2000) or the International Celestial Reference Frame (ICRS, Ma et al., 1998) catalogues, for sources within $3'$ from the aimpoint and with the Science Instrument Module Z-axis (SIM-Z) at the nominal detector value (for large off-nominal SIM-Z, the observations can suffer an additional aspect offset of up to $0''.5$).

For each source we computed two fluxes in the 0.5–10 keV range, assuming that a) the source is extragalactic and its flux was corrected for Galactic absorption (FLUX1) and b) the source is subject to no absorption (FLUX2). In general, the count-rate–

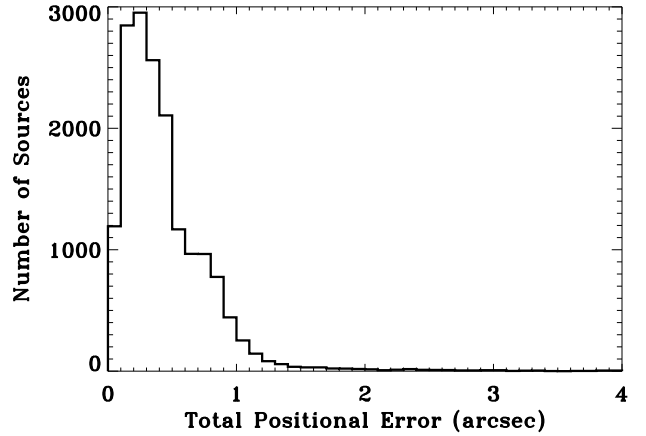


Fig. 6. Distribution of the total positional error for the 16834 BMW-*Chandra* sources that do not require a non-automated analysis. The mean is $0''.45$ and the median $0''.36$.

Table 2. Energy Bands and Background values.

Band	Energy (keV)	Background value ^a (counts s ⁻¹ chip ⁻¹)
SB	0.5-2.0	...
HB	2.0-7.0	...
FB	0.5-0.7	...
SB1	0.5-1.0	0.0336
SB2	1.0-2.0	0.0417
HB1	2.0-4.0	0.0508
HB2	4.0-7.0	0.0656

^a ACIS Background Memos: Baganoff (1999); Markevitch (2001).

to-flux conversion factors (CF) are a function of the assumed shape of the spectrum of the source. To obtain FLUX1, we first calculated an average line-of-sight column density N_H according to Dickey & Lockman (1990) with the `nH` tool in `HEASoft` (`NH_WAVG`), for each catalogue field. We show the distribution of column densities in Fig. 7. Then we performed simulations with `XSPEC` (Arnaud 1996) assuming as input model an absorbed (`wabs`) power law with photon index 2.0 (a Crab spectrum, for direct comparison with other work, e.g., the BMW-HRI catalogue; Panzera et al. 2003) for a range of column densities spanning these values. We report the model 0.5–7.0 keV count rate to 0.5–10 keV flux CFs in the catalogue column `COR_FAC1`, while the flux was calculated as $FLUX1 = COR_FAC1 \times T_FT_CTS / EXPOSURE$, where `T_FT_CTS` are the WT total counts and `EXPOSURE` is the total exposure time. To calculate FLUX2 an unabsorbed ($N_H = 0$) spectrum was simulated, and the 0.5–7.0 keV count rate to 0.5–10 keV flux conversion factor is $CF2 = 8.23 \times 10^{-12} \text{ erg cm}^{-2} \text{ cts}^{-1}$.

For comparison with other work, we also report approximate fluxes in the three bands (`T_FLUX`, `S_FLUX`, and `H_FLUX`) calculated using a count rate to flux conversion factor $CF0 = 1 \times 10^{-11} \text{ erg cm}^{-2} \text{ cts}^{-1}$.

Each field was visually inspected to identify and remove obviously spurious detections (such as image streaks in correspondence of bright pointed sources and crowded fields, an example of which is shown in Figs. 4 and 5). A number of checks

⁵ The most updated information on the *Chandra* absolute positional accuracy can be found at <http://cxc.harvard.edu/cal/ASPECT/celmon/>.

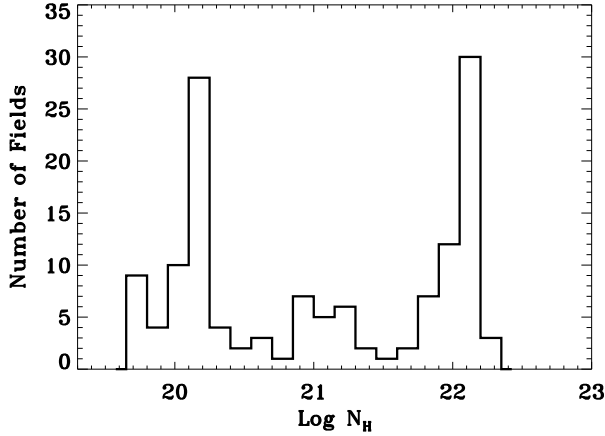


Fig. 7. Distribution of the Galactic column density of the 136 observations according to Dickey & Lockman (1990).

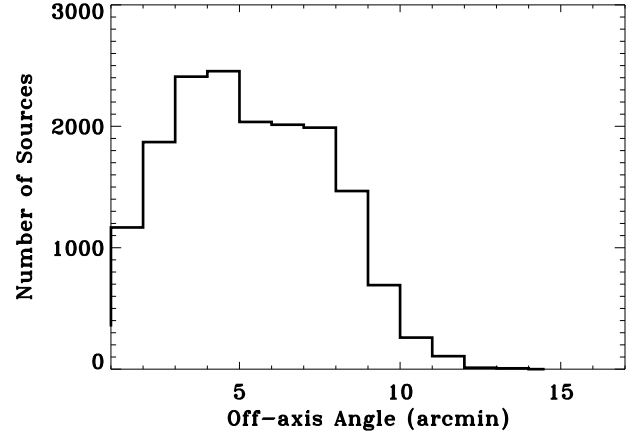


Fig. 8. Distribution of the off-axis angle of the 16834 BMW-*Chandra* sources.

were performed on the raw catalogue and the results stored in the FL_CHECK catalogue column, as follows.

1. We eliminated sources that presented negative fitted counts (an instance that may occur if the WT fit does not converge).
2. When the errors on position, the total positional error, and the error on the width (X_POS_ER, Y_POS_ER, T_POS_ER, WIDTH_ER, respectively), did not converge, they were set to their statistical value (FL_CHECK = -2), if possible, otherwise the sources were eliminated.
3. When the error on the width exceeded the width value (WIDTH), it was set to the statistical value (FL_CHECK = -2), if possible, otherwise it was left unmodified (FL_CHECK = -3).
4. When the error on the rate (T_CR_ER, S_CR_ER, H_CR_ER) exceeded the rate value (T_CTRATE, S_CTRATE, H_CTRATE), it was set to its statistical value (FL_CHECK = -2), if possible, otherwise it was left unmodified (FL_CHECK = -4).
5. When the fitted counts (T_FT_CTS, S_FT_CTS, H_FT_CTS), and count rates (T_CTRATE, S_CTRATE, H_CTRATE), and consequently, the fluxes (FLUX1, FLUX2), resulted infinite (because the WT fit did not converge), they were set to -9999.9.

Each field was visually inspected again to exclude/flag problematic portions, and the results stored in the FL_CHK2 catalogue column. In particular, extended pointed targets were flagged (FL_CHK2 = -1). Sources within a radius of 30'' from the target position (as given by RA_TARG and DEC_TARG original header fields) of all fields not in surveys (73) were flagged with FL_CHK2 = 10 × FL_CHK2.

The parameters of the final catalogue are listed in Table 3. The full catalogue contains 21325 sources, 16834 of which do not require a more in-depth, non-automated analysis (i.e. not associated with bright and/or extended sources at the centre of the field). The latter are obtained applying the following conditions, FL_CHK2 ≠ -1, and FL_CHK2 ≠ -10, and include the pointed ones. The final number of sources not associated with pointed targets is 16758 (see Sect. 5.1).

5. Source properties and sub-samples

The full catalogue includes all detections in the 136 examined fields, and no association was made among the sources detected more than once in different observations of the same portion of the sky. In order to account for repeated detections and to exploit multiple detections of the same source in variability studies, an estimate of the number of independent source detections is needed. We estimated this number by cross matching the catalogue with a given cross-matching radius, i.e., by merging the number of sources within the cross-matching radius. Given the distribution of total position uncertainties (Fig. 6), we chose cross-matching radii of 3'' and 4.5'' (catalogue parameters CORR_RAD and CORR_RA2, respectively). We obtain 16088 independent sources in the former case, and 15497 in the latter case (of which 12135 and 11954, respectively, are not associated with bright and/or extended sources at the centre of the field). The catalogue parameter FL_MERGE assumes the value 1 if the source is part of the sub-sample merged within CORR_RAD, 0 otherwise. FL_MERG2 is the corresponding value for CORR_RA2.

5.1. The serendipitous source catalogue (BMC-SSC)

For cosmological studies it is particularly important to have a sample which is not biased toward objects selected on the basis of their properties. To this end, we selected a subsample of the BMW-C catalogue that contains 16758 sources not associated with pointed targets, by excluding sources within a radius of 30'' from the target position. This subsample represents the BMW-*Chandra* Serendipitous Source Catalogue (BMC-SSC).

5.2. Source extension

Figure 8 shows the distribution of the source off-axis angle OFFAX, which presents a steep increase with collecting area, and a gentler decrease with decreasing sensitivity with off-axis angles. Differently from what found with the BMW-HRI catalogue (Panzer et al. 2003), our distribution does not present a peak at zero off-axis due to pointed sources.

To characterise the source extension, which is one of the main features of the WT method, one cannot simply compare the WT width with the instrumental PSF at a given off-axis angle. Thus, we use a σ -clipping algorithm which divides the dis-

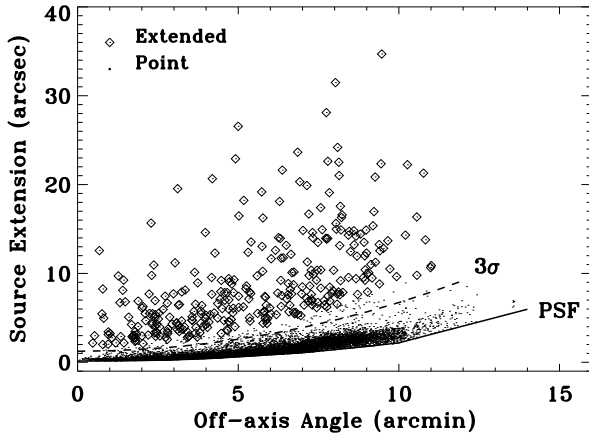


Fig. 9. Extension of the 12648 BMW-*Chandra* sources as a function of the off-axis angle. The dashed line is the 3σ limit for point sources. Diamonds are the extended sources ($\sim 4.5\sigma$), i.e., sources that lie more than 2σ from the dashed line (316 points).

tribution of source extensions as a function of off-axis angle in bins of $1'$ width. The mean and standard deviation are calculated within each bin and all sources which width exceeds 3σ the mean value are discarded. The procedure is repeated until convergence is reached. The advantage of this method is that it effectively eliminates truly extended sources, while providing a value for the mean and standard deviation in each bin (Lazzati et al. 1999). The mean value plus the 3σ dispersion⁶ provides the line discriminating the source extension, but we conservatively classify as extended only the sources that lie 2σ above this limit. Combining this threshold with the 3σ on the intrinsic dispersion, we obtain a $\sim 4.5\sigma$ confidence level for the extension classification (Rosati et al. 1995; Campana et al. 1999; Panzera et al. 2003). We note (Moretti et al. 2004) that fluxes of extended sources are usually underestimated, since they are computed by fitting a Gaussian to the surface brightness profile, which in many cases is a poor approximation.

We applied the σ -clipping algorithm to the 12648 good sources which WT width had been successfully determined (i.e., the width had not been fixed to the PSF value, $W_FLAG = 1$). Figure 9 shows their extension thus calculated as a function of the off-axis angle, as well as the PSF function and 3σ limit for point sources (dashed line). Diamonds are the extended sources ($\sim 4.5\sigma$), i.e., sources that lie more than 2σ from the dashed line (316 points). There are 145 points within the 3 and 4.5σ limits.

We selected two sub-catalogues, based on Galactic latitude, the discriminant value being 20° , thus obtaining 7401 high-latitude sources, and 9433 low-latitude sources. Figure 10 shows the distribution of the extension of the extended sources for the full sample (solid line, 316 sources) and for the high-latitude sub-sample (dotted line, 120 sources). We expect that most high-galactic latitude sources are extra-galactic. Table 4 summarises the basic numbers of sources in each subsample examined.

⁶ The fitting function is the third-order polynomial: 3σ extension (arcsec) = $1.24097 + 0.0530598 \text{ OFFAX}^2 + 0.000179786 \text{ OFFAX}^3$, where OFFAX is in arcmin.

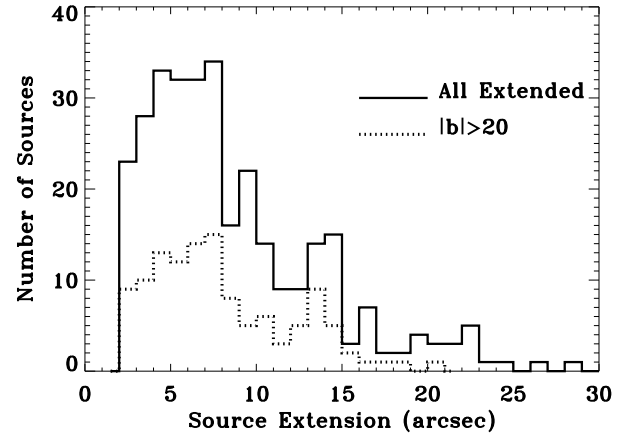


Fig. 10. Distribution of the extension of the extended sources for the full sample (solid line, 316 sources) and for the high-latitude sub-sample (dotted line, 120 sources).

Table 4. BMW-C Basic Numbers.

Source Sample		Number
detected		21325
good ^a		16834
serendipitous		16758
independent	(CORR_RAD = $3''$)	12135
	(CORR_RA2 = $4''.5$)	11954
detected in total band		11124
detected in soft band		12631
detected in hard band		9775
only detected in hard band		4203
high-latitude	($ b > 20^\circ$)	7401
	not pointed	7381
	not in surveys	2931
	not in surveys or pointed	2911
low-latitude	($ b < 20^\circ$)	9433
	not pointed	9377
	not in surveys	9433
	not in surveys or pointed	9377
serendipitous extended		316
	($ b > 20^\circ$)	120
	($ b < 20^\circ$)	196

^a Sources which do not require a more in-depth, non-automated analysis (i.e. not associated with bright and/or extended sources at the centre of the field), including the target ones.

5.3. Source fluxes

Figure 11 shows the distributions of 0.5–10 keV absorption corrected flux (FLUX1, see Sect. 4.2) for the 16834 sources in the BMW-*Chandra* catalogue; the fluxes range from $\sim 3 \times 10^{-16}$ to 9×10^{-12} erg cm⁻² s⁻¹ with a median of 7×10^{-15} erg cm⁻² s⁻¹. Figure 11 also shows the distributions of 0.5–10 keV fluxes for the high-latitude sources (median flux 4.50×10^{-15} erg cm⁻² s⁻¹) and the low-latitude sources (median flux 1.07×10^{-14} erg cm⁻² s⁻¹). Figure 12 shows the distributions of the source counts for the total (FB, median 27.9 counts), soft (SB, median 15.7 counts), and hard (HB, median 15.3 counts) bands.

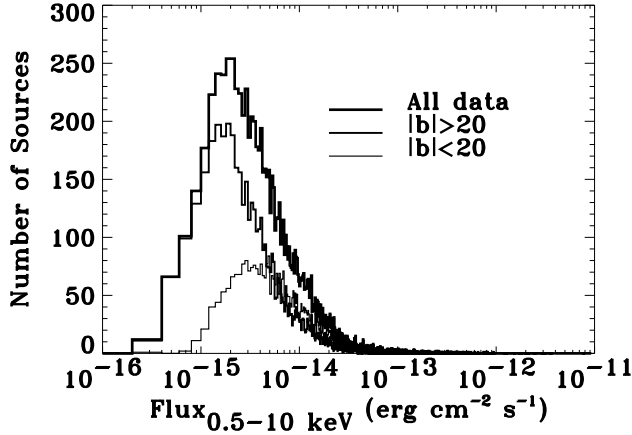


Fig. 11. Distributions of 0.5–10 keV flux for the sources in the BMW-*Chandra* catalogue (FLUX1, the Galactic absorption corrected flux), for the high-latitude sources, and the low-latitude sources.

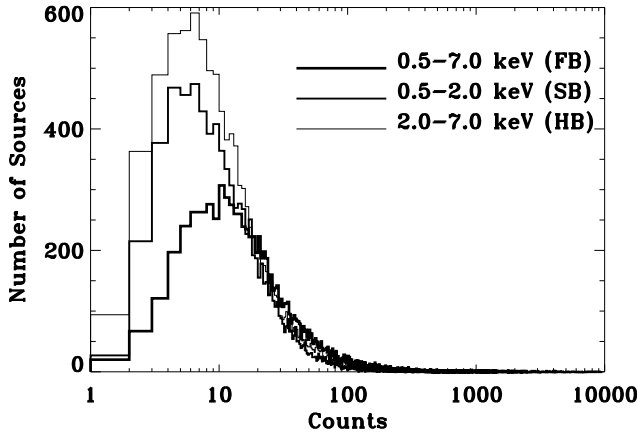


Fig. 12. Distributions of the source counts for the soft, hard, and full bands, drawn from the full catalogue.

6. Sky coverage

In order to calculate the sky coverage of our survey, we followed the procedure used by Munro et al. (2003). The signal-to-noise ratio S/N with which we measure the counts from a source is given by $n_\sigma = N / [(N + B) + \sigma_B^2]^{1/2}$, where N is the number of counts from a source, B is the background in the source cell and σ_B is the uncertainty on the background, using the simplifying assumption of \sqrt{N} uncertainties. The background can be written as $B = ab$, where a is the area of the PSF and b is the background per pixel. Therefore, using $\sigma_B^2 = B$, the S/N becomes $n_\sigma = N / (N + 2B)^{1/2} = N / (N + 2ab)^{1/2}$. The position-dependent number of source counts for a given S/N is then,

$$S = \frac{n_\sigma^2}{2} \left[1 + \left(1 + \frac{8ab}{n_\sigma^2} \right)^{1/2} \right] \text{ [cts]} \quad (1)$$

First, an off-axis angle map is generated, then the PSF maps a are generated from the off-axis map using the psfsize table in CALDB, using the PSF images at ~ 1.50 keV for the soft band PSF and at ~ 4.51 keV for the hard band PSF. We assumed

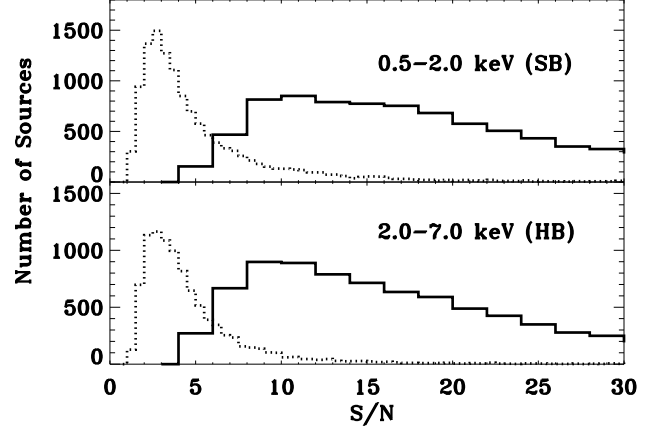


Fig. 13. S/N distribution in the counts space (dotted line) and wavelet space (solid line) in the soft (top) and hard (bottom) bands.

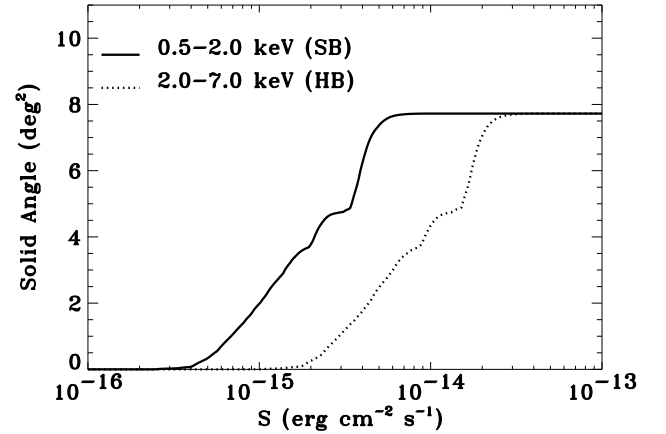


Fig. 14. Solid angle versus flux limit for $S/N = 3$ for the soft (solid line) and hard (dotted line) bands, calculated following Sect. 6. This sky coverage was constructed using 94 independent fields (no fields covered the same sky area).

as aperture the radius that encircles 70% of the PSF energy (as a reasonable compromise between having too many background counts for a larger radius and too little source counts for a smaller radius). For b we used the background images generated for the detection (see Sect. 3.1).

Based on Fig. 3, which shows the wavelet probability as a function of WT S/N , and background value, we chose $S/N = 3$ in the wavelet space, for our analysis. Figure 13 shows the S/N distribution in the counts space and wavelet space in the soft and hard bands, and demonstrates where our S/N cut falls. We note here that the S/N in WT space can be different from the S/N in counts space for several reasons: i) the background subtraction is more accurate and locally performed; ii) the high frequencies are suppressed, so that a correlated count excess gives a higher significance than a random one with the same number of counts; iii) the exposure map can be incorporated in the WT space, so that artifacts do not affect the source significance. Using Eq. 1, we calculated the limiting counts for each field, in the soft and hard bands. We then converted the limiting counts maps into limiting flux maps, using count rate-to-flux conversion factors derived

assuming a power-law model with a photon index $\Gamma = 1.7$ in the soft band and $\Gamma = 1.4$ in the hard band, modified by the absorption by Galactic N_{H} relative to each field. The adopted values of Γ were chosen to compare with the results in the literature (e.g. Kim et al. 2007a, 2004b). Histograms of the number of pixels (hence solid angle) with flux smaller than a given threshold were produced for each field in the soft and hard bands for $S/N = 3$, and the solid angle of the whole survey calculated as the sum of the contributions of each field. We note here that some of the observations covered the same sky area, notably so for the survey fields. Therefore, only the observation with the longest exposure time (after screening and correction of the data) was considered for the sky coverage calculation. In Fig. 14 we show the solid angle of the full survey (94 independent fields) as a function of the flux limit for $S/N = 3$. The complete catalogue provides a sky coverage in the soft band (0.5–2 keV, $S/N = 3$) of $\sim 8 \text{ deg}^2$ at a limiting flux of $\sim 10^{-13} \text{ erg cm}^{-2} \text{ s}^{-1}$, and $\sim 2 \text{ deg}^2$ at a limiting flux of $\sim 10^{-15} \text{ erg cm}^{-2} \text{ s}^{-1}$ (in the soft band).

7. Comparison with the ChaMP catalogue

The *Chandra* Multiwavelength Project (ChaMP) is a survey of serendipitous *Chandra* sources carried out by a multi-institution collaboration⁷. It covers $\sim 10 \text{ deg}^2$ at flux levels of $\sim 9 \times 10^{-16} \text{ erg cm}^{-2} \text{ s}^{-1}$ (Kim et al. 2004a,b, 2007a), and is derived from the analysis of 149 *Chandra* fields, that include both ACIS-I and ACIS-S images and a total of ~ 6800 sources.

The cross-matching of the source coordinates yields 162 matches within $1''$ and 210 within $3''$; shifting the coordinates of our source list by $1'$ and then cross-matching with the ChaMP again, we found no mismatches (a null misidentification probability). Fig. 15, shows the distribution of the angular separation between the BMW-C and ChaMP positions (Kim et al. 2007a, Table 5) for the matching objects. In Fig. 16 we show the BMW-C 0.5–2.0 keV counts versus the ChaMP 0.5–2.0 keV counts, as well as the best fit (solid line) and the bisecant of the plane (dashed line), $\text{Counts}_{\text{ChaMP}} = (1.035 \pm 0.002) + (-0.174 \pm 0.005) \text{Counts}_{\text{BMW-C}}$. Although our counts are generally higher (at the percent level) than the ones reported by ChaMP, we note a general consistence within $1-\sigma$. We also note that in general the WT algorithm is better equipped at disentangling sources in crowded fields and at low S/N .

8. Cross-match with existing databases

We cross-matched our catalogue with some of the largest catalogues available at other wavelengths, from radio to optical, namely, the Faint Images of the Radio Sky at Twenty-cm (FIRST), the Infrared Astronomical Satellite (IRAS) Point Source catalogue (PSC), the Two Micron All Sky Survey (2MASS), and the Guide Star Catalogue 2 (GSC2). Table 5 summarises the main characteristics of the catalogues we considered. In this section we report the results of the cross-match based on the closest-match criterion.

The FIRST is a survey that covers $\sim 10\,000$ square degrees of the North and South Galactic Cap, which produced images with $1''.8$ pixels, a typical rms of 0.15 mJy, a sensitivity of ~ 1 mJy, and a resolution of $5''$ (Becker et al. 1995). The 2003 release⁸ contains $\sim 800\,000$ sources and covers a total of $\sim 9\,000$ square degrees (White et al. 1997).

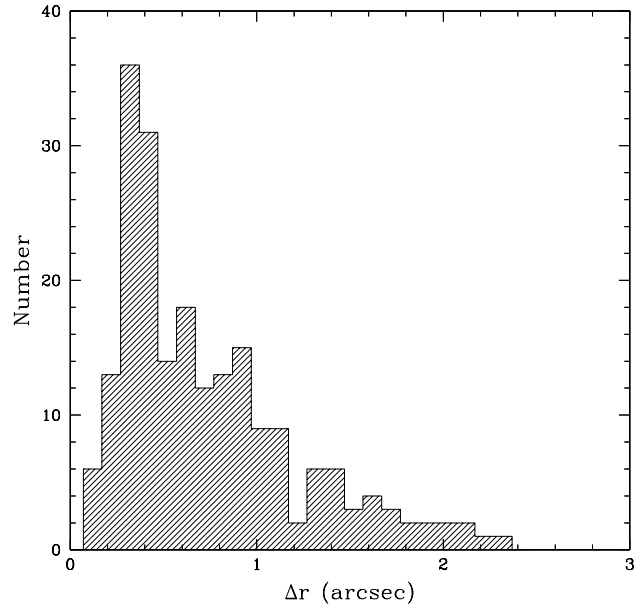


Fig. 15. BMW-C–ChaMP: distribution of the angular separation between the ChaMP and the BMW-C X-ray positions (210 matches).

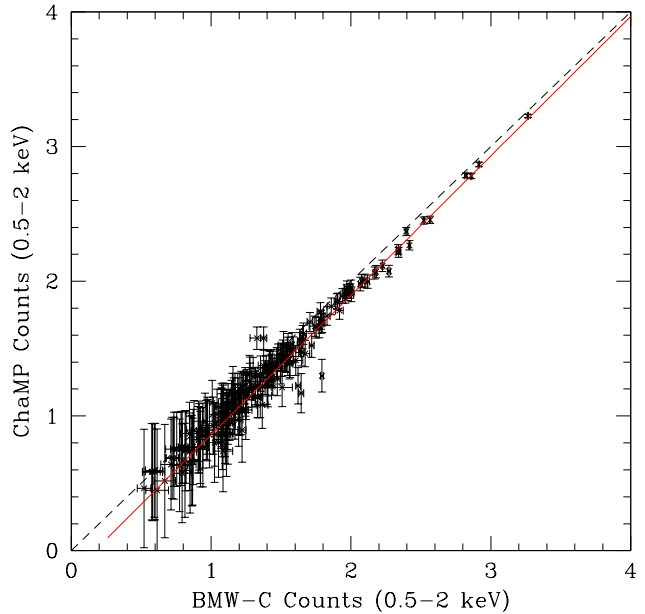


Fig. 16. BMW-C–ChaMP: the 0.5–2 keV BMW-C counts versus the 0.5–2 keV ChaMP counts (210 matches). The solid line is the best fit, while the dashed line is the bisecant of the plane.

IRAS conducted an all-sky survey at 12, 25, 60, and $100 \mu\text{m}$ that led to the IRAS Point Source catalogue (PSC). The PSC contains $\sim 250\,000$ sources (Beichman et al. 1998), and away from confused regions of the sky, is complete to $\sim 0.4, 0.5, 0.6$, and 1.0 Jy at 12, 25, 60, and $100 \mu\text{m}$, respectively, with angular resolution of $\sim 0''.5$ at $12 \mu\text{m}$ and $\sim 2''$ at $100 \mu\text{m}$. Typical po-

⁷ <http://hea-www.harvard.edu/CHAMP/>.

⁸ http://sundog.stsci.edu/first/catalogs/readme_03apr11.html.

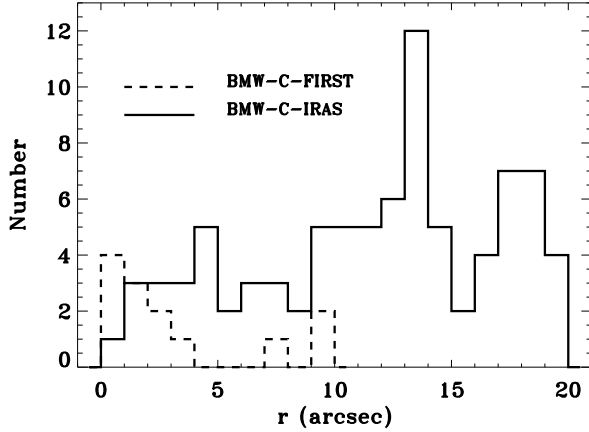


Fig. 17. Distribution of the angular separation: BMW-C-FIRST (dashed line, 13 unique matches), and BMW-C-IRAS (solid line, 87 matches).

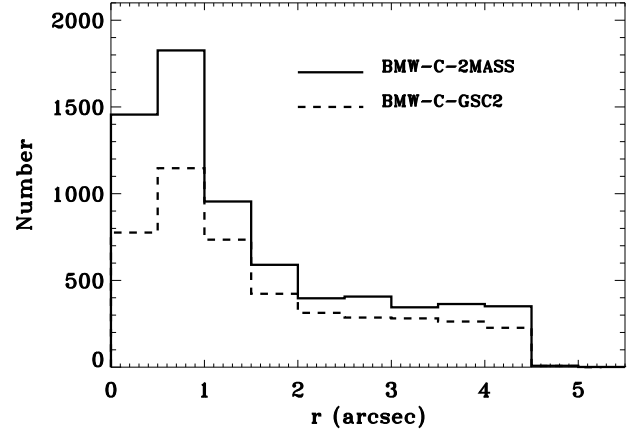


Fig. 18. Distribution of the angular separation: BMW-C-2MASS (solid line, 6700 matches) and BMW-C-GSC2 (dashed line, 4458 matches).

sition uncertainties are ~ 2 to $6''$ in-scan and about ~ 8 to $16''$ cross-scan.

The 2MASS (Skrutskie et al. 2006) covers virtually all sky with simultaneous observations in J ($1.25 \mu\text{m}$), H ($1.65 \mu\text{m}$), and K_s ($2.17 \mu\text{m}$) bands with nominal magnitude limits of 15.8, 15.1, and 14.3 mag, for point sources, and 15.0, 14.3, and 13.5 mag for extended sources, respectively. The All-Sky Data Release⁹ contains positional and photometric information for ~ 470 million point sources and ~ 1 million extended sources.

In the optical, we considered the GSC2 (Lasker et al. 2008), which is an all-sky catalogue of approximately 1 billion stars and galaxies. In particular, we used the last version (GSC2.3), which covers the entire sky in the B_J , F and N bands (roughly comparable to Johnson B , R and I bands), down to the limiting magnitudes 22.5–23, 20–22, and 19.5. Furthermore, partial sky coverage is available in the V band (similar to Johnson V filter) down to 19.5 magnitudes. The astrometry, which is calibrated with the Hipparcos (Perryman et al. 1997) and the Tycho 2 (Høg et al. 2000) catalogues is accurate to within $0''.3$. The GSC2 also provides morphological classification for objects observed at least in two bands with a $\sim 90\%$ confidence level for objects at $|b| \gtrsim 5^\circ$ and brighter than $B_J \sim 19$ mag.

The FIRST, IRAS, 2MASS, and GSC2 parameters are listed in Table 3. Our cross-match procedure consisted in matching objects in the BMW-C catalogue with objects in the other catalogues within a given cross-matching radius (Table 6), and in case of multiple matches selecting the spatially closest one. Our choice of cross-matching depended on a combination of the positioning accuracy of the BMW-C and the other catalogues. In general, more than one optical identification was available for most BMW-C objects. Table 6 shows the number of BMW-C sources that have only one, only two, or three or more matches in the other catalogues (Columns 4, 5, and 6, respectively). The table also shows the total number of matches obtained after a closest distance selection (Column 7). In Figs. 17 and 18 we show the distribution of the angular separations between the BMW-C position and the position of the other catalogues for these closest-matching objects. For the 2MASS and GSC2, the distance distribution peaks at $\sim 1''$.

There is only one BMW-C source which is found in the FIRST, IRAS, 2MASS and GSC2 catalogues (1BMC163608.2+410509); it is a galaxy observed by Infrared Space Observatory (ISO), in the European Large Area ISO Survey (ELAIS, Väisänen et al. 2002) and in the radio (Cilegi et al. 1999). Furthermore, 71 BMW-C sources have IRAS, 2MASS and GSC2 matches; 4208 are found in both 2MASS and GSC2 catalogues.

We calculated the expected number of mismatches (Column 8 in Table 6) by shifting the coordinates of our source list by $1'$ and then cross-matching with the other catalogues again.

9. Summary and future work

We presented the BMW-C source catalogue drawn from 136 *Chandra* ACIS-I pointed observations with an exposure time in excess of 10 ks public as of March 2003. The full catalogue comprises 21325 sources, 16834 of which do not require a more in-depth, non-automated analysis (i.e. not associated with bright and/or extended sources), including the pointed ones. Among them, 16758 are serendipitous. This makes our catalogue the largest compilation of *Chandra* sources to date. The 0.5–10 keV absorption corrected fluxes of these sources range from $\sim 3 \times 10^{-16}$ to $9 \times 10^{-12} \text{ erg cm}^{-2} \text{ s}^{-1}$ with a median of $7 \times 10^{-15} \text{ erg cm}^{-2} \text{ s}^{-1}$.

The catalogue includes count rates and relative errors in three energy bands (total, 0.5–7 keV; soft, 0.5–2 keV; and hard band, 2–7 keV; the source positions are relative to the highest signal-to-noise detection among the three bands), as well as source counts extracted in four additional energy bands, SB1 (0.5–1 keV), SB2 (1.0–2.0 keV), HB1 (2.0–4.0 keV) and HB2 (4.0–7.0 keV), and information drawn from the headers of the original files. The WT algorithm also provides an estimate of the extension of the source which we refined with a σ -clipping method.

We computed the sky coverage for the full catalogue and for a subset at high Galactic latitude ($|b| > 20^\circ$). The complete catalogue provides a sky coverage in the soft band (0.5–2 keV, $S/N=3$) of $\sim 8 \text{ deg}^2$ at a limiting flux of $\sim 10^{-13} \text{ erg cm}^{-2} \text{ s}^{-1}$, and $\sim 2 \text{ deg}^2$ at a limiting flux of $\sim 10^{-15} \text{ erg cm}^{-2} \text{ s}^{-1}$.

We also presented the results of the cross-match with existing catalogues at different wavelengths (FIRST, IRAS, 2MASS, GSC2 and ChaMP).

⁹ <http://www.ipac.caltech.edu/2mass/releases/allsky/index.html>.

Among the scientific applications of the catalogue are: 1) search for periodic and non-periodic variability using light curves extracted for bright sources; 2) the optical/IR follow-up of a list of galaxy cluster candidates drawn from our sub-sample of ~ 300 extended sources; 3) analysis of blank fields, i.e. X-ray detected sources without counterparts at other wavelengths; 4) optical/IR follow-up of peculiar sources, such as isolated neutron stars candidates (ultra-soft sources) and heavily absorbed sources (ultra-hard sources, not observed in the soft bands).

The current version of the BMW-C source catalogue, (as well as additional information and data) is available at the Brera Observatory site: <http://www.brera.inaf.it/BMC/bmc.home.html>.

Acknowledgements. We thank the anonymous referee for insightful comments that improved our paper. This work was supported through Consorzio Nazionale per l'Astronomia e l'Astrofisica (CNAO) and Ministero dell'Istruzione, dell'Università e della Ricerca (MIUR) grants. We thank A. Mistò for his help with the database software. This publication makes use of data products from the *Chandra* Data Archive, the FIRST, IRAS, 2MASS, GSC2 surveys.

References

- Arnaud, K. A. 1996, ASP Conf. Ser. 101: Astronomical Data Analysis Software and Systems V, 5, 17
- Baganoff, F. 1999, ACIS Background Memo: 09/01/99, http://cxc.harvard.edu/cal/Links/Acis/acis/Cal_prods/bkgnd/current/
- Becker, R. H., White, R. L., & Helfand, D. J. 1995, ApJ, 450, 559
- Beichman C. A., et al. 1988, IRAS Catalogs and Atlases, vol 1, Explanatory Supplement, ed. Beichman C., Neugebauer G., Habing H. J., Clegg P. E., and Chester T. J. NASA RP-1190, (Washington, DC: GPO)
- Bijaoui, A. & Giudicelli, M. 1991, Experimental Astronomy, 1, 347
- Blackburn, J. K. 1995, ASP Conf. Ser. 77: Astronomical Data Analysis Software and Systems IV, 4, 367
- Campana, S., Lazzati, D., Panzera, M. R., & Tagliaferri, G. 1999, ApJ, 524, 423
- Campana, S., Moretti, A., Lazzati, D., & Tagliaferri, G. 2001, ApJ, 560, L19
- Chierigato, M., Campana, S., Treves, A., et al. 2005, A&A, 444, 69
- Ciliegi, P., McMahon, R. G., Miley, G., et al. 1999, MNRAS, 302, 222
- Damiani, F., Maggio, A., Micela, G., & Sciortino, S. 1997, ApJ, 483, 350
- Damiani, F., Maggio, A., Micela, G., & Sciortino, S. 1997, ApJ, 483, 370
- Dickey, J. M., & Lockman, F. M. 1990, ARA&A, 28, 215
- Freeman, P. E., Kashyap, V., Rosner, R., & Lamb, D. Q. 2002, ApJS, 138, 185
- Grebenev, S. A., Forman, W., Jones, C., & Murray, S. 1995, ApJ, 445, 607
- Høg, E., Fabricius, C., Makarov, V. V., et al. 2000, A&A, 355, L27
- Kim, D. -W., Cameron, R. A., Drake, J. J., et al. 2004a, ApJS, 150, 19
- Kim, D. -W., Wilkes, B. J., Green, P. J., et al. 2004b, ApJ, 600, 59
- Kim, M., Kim, D. -W., Wilkes, B. J., et al., 2007, ApJS, 169, 401
- Kim, M., Wilkes, B. J., Kim, D. -W., et al., 2007, ApJ, 659, 29
- Lazzati, D., Campana, S., Rosati, P., Chincarini, G., & Giacconi, R. 1998, A&A, 331, 41
- Lazzati, D., Campana, S., Rosati, P., Panzera, M. R., & Tagliaferri, G. 1999, ApJ, 524, 414
- Markevitch, M. 2001, ACIS Background Memo: 09/28/01, <http://cxc.harvard.edu/contrib/maxim/bg/index.html>
- Marshall, F. E., Boldt, E. A., Holt, S. S., et al., 1980, ApJ, 235, 4
- Lasker, B. M., Lattanzi, M. G., McLean, B. J., et al., 2008, AJ, in press
- Ma, C., et al. 1998, AJ, 116, 516
- Moretti, A., Lazzati, D., Campana, S., & Tagliaferri, G. 2002, ApJ, 570, 502
- Moretti, A., Campana, S., Lazzati, D., & Tagliaferri, G. 2003, ApJ, 588, 696
- Moretti, A., Guzzo, L., Campana, S., et al., 2004, A&A, 428, 21
- Muno, M. P., Baganoff, F. K., Bautz, M. W., et al. 2003, ApJ, 589, 225
- Panzera, M. R., Campana, S., Covino, S., et al., 2003, A&A, 399, 351
- Perryman, M. A. C., Lindegren, L., Kovalevsky, J., et al. 1997, A&A, 323, L49
- Pislar, V., Durret, F., Gerbal, D., Lima Neto, G. B., & Slezak, E. 1997, A&A, 322, 53
- Rosati, P., della Ceca, R., Burg, R., Norman, C., & Giacconi, R. 1995, ApJ, 445, L11
- Rosati, P., della Ceca, R., Norman, C., & Giacconi, R. 1998, ApJ, 492, L21
- Slezak, E., Durret, F., & Gerbal, D. 1994, AJ, 108, 1996
- Skrutskie, M. F., Cutri, R. M., Stiening, R., et al., 2006, AJ, 131, 1163 IAUID, 13, 49
- Tajer, M., Trinchieri, G., Wolter, A., et al., 2005, A&A, 435, 799
- Tozzi, P., Rosati, P., Nonino, M., et al. 2001, ApJ, 562, 42
- Väisänen, P., et al. 2002, MNRAS, 337, 1043
- Vikhlinin, A., McNamara, B. R., Forman, W., et al., 1998, ApJ, 502, 558
- White, R. L., Becker, R. H., Helfand, D. J., & Gregg, M. D. 1997, ApJ, 475, 479

Table 1. Field Properties in the BMW-C Sample.

ID (OBSID)	Sequence (SEQ_NUM)	Target Name (OBJECT)	Nominal RA (RA_NOM) (J2000)	Nominal Dec (DEC_NOM) (J2000)	Observation Date (DATE_OBS)	MJD	Effective Exp. (TEFF, s)	Average N_H (NH_WAVG) (10^{20} cm^{-2})
19	200017	CRACLOUDCORE	285.44943	-36.97264	2000-10-07T17:01:59	51824.7	19705.67	7.75
50	290019	ETACARINAE	161.25481	-59.68144	1999-09-06T19:49:15	51427.8	9143.05	1.36×10^2
65	290034	NGC2516	119.58374	-60.78898	1999-08-26T15:20:50	51416.6	7754.19	1.46×10^1
79	300004	NGC6397	265.17007	-53.68983	2000-07-31T15:31:33	51756.6	48343.20	1.38×10^1
88	400001	CENX-3	170.31691	-60.61832	2000-11-25T07:57:31	51873.3	35742.88	1.19×10^2
90	400003	4U1538-52	235.60481	-52.38390	2000-04-08T22:46:16	51642.9	20950.14	9.71×10^1
96	400009	GS2000+25	300.70609	25.23087	1999-11-05T11:03:12	51487.5	18836.82	6.55×10^1
322	600082	NGC4472	187.44366	8.00878	2000-03-19T12:15:22	51622.5	10363.09	1.66
324	600084	NGC4636	190.71155	2.69179	1999-12-04T23:48:01	51517.0	6296.65	1.81
441	900003	AXAFSouthernDee	53.11186	-27.80500	2000-05-27T01:18:05	51691.1	54985.14	9.00×10^{-1}
446	200036	W3B	36.41589	62.09362	2000-04-03T02:57:18	51637.1	20059.54	9.07×10^1
522	800030	A209	23.01838	-13.56364	2000-09-09T09:50:41	51796.4	9965.00	1.66
580	900001	HUBBLEDEEPPFIELD	189.31799	62.21036	1999-11-13T01:14:18	51495.1	49433.22	1.49
582	900003	AXAFSouthernDee	53.11215	-27.80473	2000-06-03T02:38:23	51698.1	128609.01	9.00×10^{-1}
606	200031	IC348	56.12549	32.13877	2000-09-21T19:58:42	51808.8	51663.77	1.37×10^1
611	200036	W3B	36.41431	62.09313	2000-03-23T11:59:55	51626.5	18467.16	9.07×10^1
633	200058	NGC3603	168.78081	-61.26516	2000-05-01T23:29:33	51666.0	46210.94	1.35×10^2
635	200060	RHOOPHCORE	246.82513	-24.57316	2000-04-13T18:33:23	51647.8	76286.52	1.40×10^1
637	200062	RHOOPHA	246.64668	-24.38723	2000-05-15T23:35:16	51680.0	96094.30	1.41×10^1
642	200067	NGC1333	52.27541	31.32702	2000-07-12T22:55:58	51738.0	36044.84	1.51×10^1
652	300021	V382Velorum1999	161.25778	-52.38171	1999-12-30T19:25:10	51542.8	14954.87	3.69×10^1
653	300022	NGC5139	201.69753	-47.47309	2000-01-24T02:15:01	51567.1	25026.24	9.43
676	400043	GROJ0422+32	65.42895	32.91309	2000-10-10T06:57:08	51827.3	18795.74	1.66×10^1
677	400044	4U1543-47	236.78270	-47.67433	2000-07-26T10:30:33	51751.4	9844.94	4.00×10^1
799	600102	NGC1395	54.65637	-23.06370	1999-12-31T06:31:53	51543.3	18983.21	1.97
868	700173	PG1115+407	169.67772	40.42151	2000-10-03T23:12:41	51821.0	17338.21	1.91
887	700192	Elais:N2	249.19620	41.02638	2000-08-02T17:43:11	51758.7	73375.76	1.07
888	700193	Elais:N1	242.58421	54.55655	2000-08-03T14:45:16	51759.6	71115.65	1.35
944	900016	SGRB2	266.78070	-28.44160	2000-03-29T09:44:36	51632.4	98629.03	1.26×10^2
945	900017	GALACTICCENTERA	266.58221	-28.87193	2000-07-07T19:05:19	51732.8	48399.41	1.10×10^2
949	900021	GALACTICPLANE	280.99377	-4.07476	2000-02-25T22:00:10	51599.9	38385.57	1.88×10^2
953	300028	47TUC	5.97537	-72.07276	2000-03-16T08:39:44	51619.4	31676.94	4.94
955	300030	47TUC	5.97539	-72.07265	2000-03-16T18:33:03	51619.8	31676.94	4.94
957	900024	HUBBLEDEEPPFIELD	189.15215	62.24523	2000-02-23T06:31:59	51597.3	57442.50	1.49
966	900026	HUBBLEDEEPPFIELD	189.26813	62.21516	1999-11-21T04:03:48	51503.2	55972.70	1.49
967	900027	HUBBLEDEEPPFIELD	189.26808	62.21466	1999-11-14T19:47:49	51496.8	57433.02	1.49
972	200079	M17	275.12656	-16.17502	2002-03-02T17:05:03	52335.7	39439.75	1.45×10^2
977	200084	NGC6530	271.10144	-24.35215	2001-06-18T11:40:26	52078.5	58008.05	7.09×10^1
978	200085	M16	274.68353	-13.80290	2001-07-30T18:55:00	52120.8	77126.02	1.24×10^2
1109	780059	PKS0312-770	47.99976	-76.86046	1999-09-08T02:42:07	51429.1	12836.97	8.20
1110	780060	PKS0312-770	48.13725	-76.84995	1999-09-08T06:48:47	51429.3	12581.05	8.20
1111	780061	PKS0312-770	48.35330	-76.83350	1999-09-08T10:38:47	51429.4	12593.69	8.17
1232	280182	NGC2516	119.58367	-60.78894	1999-08-27T07:07:36	51417.3	5728.96	1.46×10^1
1249	280199	ETACARINAE	161.25478	-59.68141	1999-09-06T23:46:37	51428.0	9630.09	1.36×10^2
1479	980429	LEONIDANTI-RADI	333.29935	-22.18443	1999-11-17T22:42:28	51499.9	19690.89	2.45
1519	300022	NGC5139	201.69749	-47.47309	2000-01-25T04:33:40	51568.2	43591.34	9.43
1523	900021	GALACTICPLANE	280.99301	-4.07539	2000-02-24T09:56:58	51598.4	54724.64	1.88×10^2
1671	900030	HDFNORTH	189.26709	62.21755	2000-11-21T13:26:31	51869.6	166146.53	1.49
1672	900031	AXAFSOUTHERNDEE	53.11979	-27.81285	2000-12-16T05:07:55	51894.2	95138.09	9.01×10^{-1}
1697	900056	ISONW#3	158.65106	57.62013	2001-05-16T12:46:50	52045.5	38863.00	5.70×10^{-1}
1698	900057	ISONW#1	158.50160	57.77004	2001-05-17T18:29:38	52046.8	72974.50	5.72×10^{-1}
1699	900058	ISONW#2	158.33333	57.62089	2001-04-30T10:59:38	52029.5	40735.17	5.74×10^{-1}
1866	200094	LYNDS1551	67.88639	18.13492	2001-07-23T05:10:11	52113.2	78926.84	1.86×10^1
1867	200095	CHAINORTHCLOUD	167.53415	-76.57798	2001-07-02T06:23:33	52092.3	66292.12	8.62

Table 1. Field Properties in the BMW-C Sample, Continued.

ID (OBSID)	Sequence (SEQ_NUM)	Target Name (OBJECT)	Nominal RA (RA_NOM) (J2000)	Nominal Dec (DEC_NOM) (J2000)	Observation Date (DATE_OBS)	MJD	Effective Exp. (TEFF, s)	Average N_H (NH_WAVG) (10^{20} cm^{-2})
1873	200101	M67	132.84630	11.82625	2001-05-31T11:19:36	52060.5	46248.46	3.94
1874	200102	ROSETTEFIELD1	97.97012	4.92848	2001-01-05T11:54:17	51914.5	14450.83	7.33×10^1
1875	200103	ROSETTEFIELD2	98.17007	4.71265	2001-01-05T17:47:55	51914.7	19506.63	7.47×10^1
1876	200104	ROSETTEFIELD3	98.32136	4.57847	2001-01-05T23:29:45	51915.0	19408.68	7.47×10^1
1877	200105	ROSETTEFIELD4	98.57216	4.46292	2001-01-06T05:11:35	51915.2	19509.79	7.41×10^1
1878	200106	NGC_2024	85.44305	-1.91993	2001-08-08T06:37:10	52129.3	74671.84	2.14×10^1
1881	200109	NGC346	14.76239	-72.17383	2001-05-15T01:55:17	52044.1	98670.55	6.23
1882	200110	MONOCEROSR2	91.96145	-6.38078	2000-12-02T23:14:19	51881.0	95348.23	2.46×10^1
1893	200121	S106FIR	306.85522	37.37556	2001-11-03T00:08:14	52216.0	44387.49	1.18×10^2
1934	400147	XTEJ1723-376	260.90622	-37.66724	2001-09-04T06:40:52	52156.3	28592.80	1.43×10^2
2232	900059	HDF-N	189.14977	62.24391	2001-02-19T14:24:58	51959.6	129242.30	1.49
2233	900060	HDF-N	189.14841	62.24338	2001-02-22T03:44:27	51962.2	62157.43	1.49
2234	900061	HDF-N	189.14441	62.24145	2001-03-02T02:00:29	51970.1	162255.00	1.49
2235	900062	XMM13HR-FIELD4	203.57935	37.82424	2001-06-08T10:37:06	52068.4	30002.42	8.49×10^{-1}
2236	900063	XMM13HR-FIELD1	203.55498	37.97983	2001-06-08T19:25:34	52068.8	29800.20	8.31×10^{-1}
2237	900064	XMM13HR-FIELD2	203.77635	37.84336	2001-06-09T04:01:09	52069.2	29797.05	8.47×10^{-1}
2238	900065	XMM13HR-FIELD3	203.75237	37.99891	2001-06-09T12:36:44	52069.5	18884.53	8.32×10^{-1}
2239	900066	CDFS	53.11699	-27.81122	2000-12-23T17:28:01	51901.7	129740.39	9.00×10^{-1}
2240	900067	CADIS01HFIELD	26.90029	2.32900	2001-01-26T18:36:47	51935.8	26702.29	3.03
2252	900079	WHDF	5.63854	0.34335	2001-01-06T11:36:05	51915.5	71220.99	2.67
2254	900081	3C295	212.82706	52.20298	2001-05-18T15:25:59	52047.6	89236.41	1.33
2255	900082	NGC55	3.79150	-39.22025	2001-09-11T06:25:05	52163.3	58576.13	1.72
2267	900094	GCS20	266.17123	-29.27356	2001-07-19T10:01:48	52109.4	10208.63	1.19×10^2
2268	900095	GCS21	265.98087	-29.17148	2001-07-20T04:37:11	52110.2	10811.74	1.16×10^2
2270	900097	GCS22	266.24515	-29.54168	2001-07-20T08:00:49	52110.3	10622.17	1.23×10^2
2272	900099	GCS23	266.05414	-29.43966	2001-07-20T11:12:40	52110.5	11611.05	1.26×10^2
2273	900100	GCS10	266.71024	-28.87570	2001-07-18T00:48:28	52108.0	11611.05	1.11×10^2
2274	900101	GCS3	266.67642	-28.17316	2001-07-16T08:44:25	52106.4	10426.28	1.29×10^2
2275	900102	GCS24	265.86353	-29.33749	2001-07-20T14:41:10	52110.6	11598.25	1.22×10^2
2276	900103	GCS11	266.52002	-28.77435	2001-07-18T04:16:58	52108.2	11520.58	1.13×10^2
2277	900104	GCS4	266.94061	-28.54206	2001-07-16T11:52:55	52106.5	10426.28	1.22×10^2
2278	900105	GCS25	266.12796	-29.70796	2001-07-20T18:09:40	52110.8	10030.49	1.30×10^2
2279	900106	GCS12	266.33029	-28.67280	2001-07-18T07:45:28	52108.3	11611.05	1.10×10^2
2280	900107	GCS5	266.75079	-28.44106	2001-07-16T15:01:25	52106.6	10426.28	1.26×10^2
2281	900108	GCS26	265.93677	-29.60579	2001-07-20T21:38:10	52110.9	8219.31	1.32×10^2
2282	900109	GCS13	266.59457	-29.04224	2001-07-18T11:13:58	52108.5	10625.33	1.07×10^2
2283	900110	GCS27	265.74591	-29.50336	2001-07-21T01:06:39	52111.0	11614.25	1.29×10^2
2284	900111	GCS14	266.40414	-28.94089	2001-07-18T14:25:48	52108.6	10625.33	1.09×10^2
2285	900112	GCS6	266.56137	-28.33985	2001-07-16T18:09:55	52106.8	10410.49	1.22×10^2
2286	900113	GCS28	266.01025	-29.87408	2001-07-21T04:35:09	52111.2	11614.25	1.37×10^2
2287	900114	GCS15	266.21411	-28.83905	2001-07-18T17:37:38	52108.7	10625.33	1.07×10^2
2288	900115	GCS7	266.82550	-28.70883	2001-07-17T14:11:51	52107.6	11493.24	1.17×10^2
2289	900116	GCS29	265.81894	-29.77175	2001-07-21T08:03:39	52111.3	11614.25	1.40×10^2
2290	900117	GCS30	265.62793	-29.66920	2001-07-21T11:32:10	52111.5	11614.25	1.36×10^2
2291	900118	GCS16	266.47845	-29.20889	2001-07-18T20:49:28	52108.9	10625.33	1.11×10^2
2292	900119	GCS8	266.63556	-28.60780	2001-07-17T17:51:28	52107.7	11604.73	1.19×10^2
2293	900120	GCS17	266.28790	-29.10730	2001-07-19T00:01:18	52109.0	11118.21	1.13×10^2
2294	900121	GCS9	266.44598	-28.50635	2001-07-17T21:19:58	52107.9	11611.05	1.16×10^2
2295	900122	GCS18	266.09775	-29.00538	2001-07-19T03:21:28	52109.1	11118.21	1.10×10^2
2296	900123	GCS19	266.36200	-29.37541	2001-07-19T06:41:38	52109.3	11118.21	1.17×10^2
2298	900125	GALACTICPLANE1	280.88382	-3.90722	2001-05-20T08:44:32	52049.4	94214.80	2.00×10^2
2300	900127	1RXSJ104047.4-7	160.18372	-70.78441	2001-09-11T02:20:34	52163.1	12802.17	1.05×10^1
2312	900066	CDFS	53.11796	-27.81074	2000-12-13T03:28:03	51891.1	123686.25	9.00×10^{-1}
2313	900066	CDFS	53.11699	-27.81122	2000-12-21T02:08:43	51899.1	130389.61	9.00×10^{-1}

Table 1. Field Properties in the BMW-C Sample, Continued.

ID (OBSID)	Sequence (SEQ_NUM)	Target Name (OBJECT)	Nominal RA (RA_NOM) (J2000)	Nominal Dec (DEC_NOM) (J2000)	Observation Date (DATE_OBS)	MJD	Effective Exp. (TEFF, s)	Average N_H (NH_WAVG) (10^{20} cm^{-2})
2344	900030	HDFNORTH	189.26715	62.21756	2000-11-24T05:41:51	51872.2	66696.32	1.49
2386	900030	HDFNORTH	189.26720	62.21756	2000-11-20T05:39:48	51868.2	9842.40	1.49
2405	900031	AXAFSOUTHERNDEE	53.12021	-27.81259	2000-12-11T08:14:17	51889.3	56702.80	9.01×10^{-1}
2406	900066	CDFS	53.11819	-27.81062	2000-12-10T23:35:12	51889.0	29686.29	9.00×10^{-1}
2409	900066	CDFS	53.11699	-27.81123	2000-12-19T03:55:35	51897.2	68982.46	9.00×10^{-1}
2421	900061	HDF-N	189.14301	62.24069	2001-03-04T16:52:28	51972.7	61648.85	1.49
2423	900060	HDF-N	189.14841	62.24339	2001-02-23T06:57:57	51963.3	68419.52	1.49
2550	200158	NGC2264	100.19905	9.84542	2002-02-09T05:10:47	52314.2	48137.83	4.70×10^1
2553	200161	MADDALENA'SCLOU	102.27326	-4.56858	2002-02-08T20:39:21	52313.9	20757.27	7.54×10^1
2556	200164	RCW38	134.83614	-47.50389	2001-12-10T10:14:38	52253.4	95599.90	8.93×10^1
2562	200170	IRAM04191	65.48610	15.49148	2002-02-09T19:08:44	52314.8	18918.96	1.80×10^1
3293	900132	HDF-N	189.21547	62.21753	2001-11-13T15:04:42	52226.6	161250.19	1.49
3294	900133	HDF-N	189.15369	62.24493	2002-02-14T03:22:07	52319.1	166971.55	1.49
3305	900144	GROTH-WESTPHALF	214.42932	52.47367	2002-08-11T21:43:57	52497.9	29405.28	1.28
3343	900182	LH-NW-6	158.33452	57.92092	2002-05-03T09:11:41	52397.4	31812.35	5.91×10^{-1}
3344	900183	LH-NW-7	158.18425	57.77091	2002-05-01T20:03:06	52395.8	38545.61	5.89×10^{-1}
3345	900184	LH-NW-4	158.01767	57.62109	2002-04-29T03:23:45	52393.1	38466.62	5.89×10^{-1}
3346	900185	LH-NW-5	158.50150	57.47105	2002-04-30T02:03:59	52394.1	38207.51	5.73×10^{-1}
3347	900186	LH-NW-8	158.65106	57.92095	2002-05-02T14:16:27	52396.6	38463.43	5.72×10^{-1}
3348	900187	LH-NW-9	158.80956	57.77088	2002-05-04T11:01:47	52398.5	39521.85	5.69×10^{-1}
3388	900132	HDF-N	189.21545	62.21752	2001-11-16T05:41:16	52229.2	49560.66	1.49
3389	900132	HDF-N	189.21523	62.21782	2001-11-21T14:16:05	52234.6	102258.35	1.49
3390	900133	HDF-N	189.15369	62.24493	2002-02-16T18:58:56	52321.8	161733.11	1.49
3391	900133	HDF-N	189.15369	62.24493	2002-02-22T01:52:24	52327.1	164732.22	1.49
3408	900132	HDF-N	189.21547	62.21753	2001-11-17T01:09:01	52230.0	66213.38	1.49
3409	900133	HDF-N	189.15367	62.24494	2002-02-12T10:59:50	52317.5	82233.02	1.49
4357	900144	GROTH-WESTPHALF	214.42932	52.47367	2002-08-12T22:32:00	52498.9	84361.27	1.28
4365	900144	GROTH-WESTPHALF	214.42934	52.47367	2002-08-21T10:56:53	52507.5	58854.59	1.28

Table 3. BMW-C Parameters

Column	BMWC Parameter	Description
1	UNIQ_NUM	source unique number (internal reference)
2	SRC_NAME	source IUA name BMCHHMMSS.S \pm DDMMSS
3	SEQ_NUM	sequence Number of the Observation (e.g., 900030)
4	OBJECT	target name (e.g., HDFNORTH)
5	OBS_ID	observation ID Number of the Target (e.g., 2386)
6	EXPOSURE	total exposure time (s)
7	EXPTIME	commanded exposure time (s)
8	ASCDSVER	ASCDS version number (e.g., 6.0.1)
9	DATE_OBS	date and time of observation start (e.g., 2000-11-20T05:39:48)
10	DATE_END	date and time of observation stop (e.g., 2000-11-20T08:54:42)
11	RA_NOM	nominal target right ascension (RA; J2000, degrees)
12	DEC_NOM	nominal target declination (DEC; J2000, degrees)
13	OBS_MODE	observation mode (e.g., POINTING)
14	DATAMODE	data mode (e.g., FAINT)
15	READMODE	read mode (e.g., TIMED)
16	TEFF	effective exposure (s, after flares are removed)
17	T_BCK	total-band mean background in the central 1024×1024 pix region (cts/pix)
18	S_BCK	soft-band mean background in the central 1024×1024 pix region (cts/pix)
19	H_BCK	hard-band mean background in the central 1024×1024 pix region (cts/pix)
20	NH_WAVG	weighted averaged N_H (cm^{-2}) for RA_NOM, DEC_NOM
21	COR_FAC1	($\text{erg cm}^{-2} \text{cts}^{-1}$), counts(0.5–7 keV) vs. Flux(0.5–10 keV) for field N_H
22	SRC_RA_H	source RA (hh)
23	SRC_RA_M	source RA (mm)
24	SRC_RA_S	source RA (ss)
25	SRC_DEC_D	source DEC (dd)
26	SRC_DEC_M	source DEC (mm)
27	SRC_DEC_S	source DEC (ss)
28	SRC_ALPH	source RA (J2000, degrees)
29	SRC_DELT	source DEC (J2000, degrees)
30	X_POS_ER	error on source RA (arcsec)
31	Y_POS_ER	error on source DEC (arcsec)
32	T_POS_ER	total positional error (arcsec)
33	WIDTH	width of WT Gaussian distribution of photons (arcsec)
34	WIDTH_ER	error on width (arcsec)
35	W_FLAG	meaningfulness of width (0/1; 0=free, 1 =fixed to PSF)
36	SCALE	scale at which source was found (1,2,4,8,16,32,64 pixels)
37	CHI2	fit χ^2
38	OFFAX	offaxis angle (arcmin)
39	X_POS	source x-coordinate (pixel)
40	Y_POS	source y-coordinate (pixel)
41	T_FT_CTS	total-band (0.5–7 keV) counts from the fit (cts)
42	T_CTS_ER	total-band error on counts from the fit (cts)
43	T_CN_CTS	total-band net counted source counts (cts)
44	T_CN_BG	total-band counted background counts (cts)
45	T_VIGCOR	total-band vignetting correction factor
46	T_PSF COR	total-band PSF correction factor
47	T_CTRATE	total-band count rate (cts s^{-1})
48	T_CR_ER	total-band count rate error (cts s^{-1})
49	T_FLUX	total-band flux (for CF0= $1 \times 10^{-11} \text{ erg cm}^{-2} \text{cts}^{-1}$)
50	T_FT_S_N	total-band signal-to-noise ratio of the detection
51	T_WV_S_N	total-band signal-to-noise ratio in wavelet space
52	S_FT_CTS	soft-band (0.5–2 keV) counts from the fit (cts)
53	S_CTS_ER	soft-band error on counts from the fit (cts)
54	S_CN_CTS	soft-band net counted source counts (cts)
55	S_CN_BG	soft-band counted background counts (cts)
56	S_VIGCOR	soft-band vignetting correction factor
57	S_PSF COR	soft-band PSF correction factor
58	S_CTRATE	soft-band count rate (cts s^{-1})
59	S_CR_ER	soft-band count rate error (cts s^{-1})
60	S_FLUX	soft-band flux (for CF0= $1 \times 10^{-11} \text{ erg cm}^{-2} \text{cts}^{-1}$)
61	S_FT_S_N	soft-band signal-to-noise ratio of the detection
62	S_WV_S_N	soft-band signal-to-noise ratio in wavelet space

Table 3. BMW-C Parameters (Continued)

Column	BMWC Parameter	Description
63	H_FT_CTS	hard-band (2–7 keV) counts from the fit (cts)
64	H_CTS_ER	hard-band error on counts from the fit (cts)
65	H_CN_CTS	hard-band net counted source counts (cts)
66	H_CN_BG	hard-band counted background counts (cts)
67	H_VIGCOR	hard-band vignetting correction factor
68	H_PSF_COR	hard-band PSF correction factor
69	H_CTRATE	hard-band count rate (cts s ⁻¹)
70	H_CR_ER	hard-band count rate error (cts s ⁻¹)
71	H_FLUX	hard-band flux (for CF0= 1×10^{-11} erg cm ⁻² cts ⁻¹)
72	H_FT_S_N	hard-band signal-to-noise ratio of the detection
73	H_WV_S_N	hard-band signal-to-noise ratio in wavelet space
74	FL_REBIN	rebin at which source was found (e.g., 1/2)
75	WT_PROBAB	WT Probability
76	FLUX1	absorption corrected 0.5–10 keV flux (for COR_FAC1(NH_WAVG))
77	FLUX2	observed 0.5–10 keV flux (for CF2($N_H = 0$)= 8.22981×10^{-12} erg cm ⁻² cts ⁻¹)
78	FL_CHECK	quality flag: = 1 status ok; < -1 decreasing quality
79	FL_CHK2	quality flag: -1 = to be visually inspected, < -1 decreasing quality; > 10 pointed source
80	FL_EXT_Y	flag for extension (Point/Extended)
81	CORR_RAD	cross-matching radius
82	FL_MERGE	cross-matching: part of merged catalogue? ≥ 1 =yes, 0 =no
83	CORR_RA2	cross-matching radius
84	FL_MERG2	cross-matching: part of merged catalogue? ≥ 1 =yes, 0 =no
85	CAT_VERS	catalogue version
86	ID_FIRST	FIRST identification
87	RA_FIRST	FIRST RA (degrees)
88	DE_FIRST	FIRST DEC (degrees)
89	LOBF_1ST	warning flag for side-lobe source
90	PFLX_1ST	peak flux (mJy/bm)
91	IFLX_1ST	integrated Flux (mJy)
92	RMS_1ST	local noise at the source position (mJy/beam)
93	MAJ_1ST	deconvolved major axis (FWHM in arcsec; elliptical Gaussian model)
94	MIN_1ST	deconvolved min axis (FWHM in arcsec; elliptical Gaussian model)
95	PA_1ST	deconvolved position angle (degrees, east of north)
96	fMAJ_1ST	measured major axis (arcsec)
97	fMIN_1ST	measured minor axis(arcsec)
98	fPA_1ST	measured position angle (deg)
99	FIRSTBMC	angular distance between FIRST and BMW-C position (arcsec)
100	FIRSTCOM	number of FIRST cross-matches: -99 =none, 1=single, > 1 =number of matches
101	FIRSTCOV	BMW-C–FIRST cross-matching version
102	ID_IRAS	IRAS identification
103	RA_IRAS	IRAS RA (J2000, degrees)
104	DE_IRAS	IRAS DEC (J2000, degrees)
105	F12_IRAS	12 μ m flux (mJy)
106	F25_IRAS	25 μ m flux (mJy)
107	F60_IRAS	60 μ m flux (mJy)
108	F100_IRAS	100 μ m flux (mJy)
109	IRASBMC	angular distance between IRAS and BMW-C position (arcsec)
110	IRASCOM	number of IRAS cross-matches: -99 =none, 1=single, > 1 =number of matches
111	IRASCOV	BMW-C–IRAS cross-matching version
112	ID_2MASS	2MASS identification
113	RA_2MASS	2MASS RA (J2000, degrees)
114	DE_2MASS	2MASS DEC (J2000, degrees)
115	J_2MASS	2MASS <i>J</i> magnitude (mag)
116	DJ_2MASS	2MASS error on <i>J</i> magnitude (mag)
117	H_2MASS	2MASS <i>H</i> magnitude (mag)
118	DH_2MASS	2MASS error on <i>H</i> magnitude (mag)
119	K_2MASS	2MASS <i>K</i> magnitude (mag)
120	DK_2MASS	2MASS error on <i>K</i> magnitude (mag)
121	2MASSBMC	angular distance between 2MASS and BMW-C position (arcsec)
122	2MASSCOM	number of 2MASS cross-matches: -99 =none, 1=single, > 1 =number of matches
123	2MASSCOV	BMW-C–2MASS cross-matching version

Table 3. BMW-C Parameters (Continued)

Column	BMWC Parameter	Description
124	ID_GSC2	GSC2 identification
125	RA_GSC2	GSC2 RA (J2000, degrees)
126	DE_GSC2	GSC2 DEC (J2000, degrees)
127	F_GSC2	GSC2 F magnitude (mag)
128	DF_GSC2	GSC2 error on F magnitude (mag)
129	J_GSC2	GSC2 B_J magnitude (mag)
130	DJ_GSC2	GSC2 error on B_J magnitude (mag)
131	V_GSC2	GSC2 V magnitude (mag)
132	DV_GSC2	GSC2 error on V magnitude (mag)
133	N_GSC2	GSC2 N magnitude (mag)
134	DN_GSC2	GSC2 error on N magnitude (mag)
135	A_GSC2	GSC2 semi-major axis (pixels)
136	E_GSC2	GSC2 eccentricity
137	PA_GSC2	GSC2 position angle (deg)
138	C_GSC2	GSC2 class: 0=star; 1=galaxy; 2=blend; 3=non-star; 4=unclassified; 5=defect
139	GSC2BMC	angular distance between GSC2 and BMW-C position (arcsec)
140	GSC2COM	number of GSC2 cross-matches: -99 =none, 1 =single, > 1 =number of matches
141	GSC2COV	BMW-C–CSC2 cross-matching version
142	CTS05_1	0.5-1 keV counted source counts
143	CTS_1_2	1-2 keV counted source counts
144	CTS_2_4	2-4 keV counted source counts
145	CTS_4_7	4-7 keV counted source counts

Table 5. Catalogue Data for Cross-matching.

Catalogues	Wavelength	Sky fraction (%)	Entries	References
FIRST	20 cm	~ 25	811 117	White et al. (1997)
IRASPSC	12, 25, 60, 100 μ m	~ 98	~250 000	Beichman et al. (1998)
2MASS	1.25, 1.65, 2.16 μ m	all-sky	470 992 970	Skrutskie et al. (2006)
GSC2	B_J, F, N, V	all-sky (B_J, F, N)	~ 10 ⁹	Lasker et al. (2008)

Table 6. Cross-matches with other catalogues.

Catalogues	Cross-matching Radius (")	Total Matches	Single Matches	Double Matches	Multiple Matches	Closest Matches	Expected (%) Mismatches
FIRST	10	50	3	12	35	13	46
IRASPSC	20	156	51	38	67	87	49
2MASS	4.5	7 687	5881	1486	320	6700	50
GSC2	4.5	5 854	3788	962	1104	4485	33